

Monolithic-structured nickel silicide electrocatalyst for bifunctionally efficient overall water splitting

Zhenli He^a, Yuehui He^a, Yue Qiu^a, Qian Zhao^a, Zhonghe Wang^a, Xiyue Kang^a, Linping Yu^b, Liang Wu^c, Yao Jiang^{a,*}

^a State Key Laboratory of Powder Metallurgy, Powder Metallurgy Research Institute, Central South University, Changsha 410083, China

^b School of Chemistry and Chemical Engineering, Changsha University of Science and Technology, Changsha 410114, China

^c School of Mechanical Engineering and Mechanics, Xiangtan University, Xiangtan 411105, China



ARTICLE INFO

Keywords:

Porous monolith electrocatalyst
Nickel silicide
Bifunctional electrocatalysts
Alkaline water splitting
Molybdenum doping

ABSTRACT

The rational design and synthesis of cost-effective and efficient bifunctional electrocatalysts are crucial for developing hydrogen energy yet challenging. Here we report porous monolith electrocatalysts (PMECs) comprising transition metal silicide (e.g., nickel silicide) with high activity and durability. These PMECs offer strong synergistic effects and high exposure of active sites, resulting in excellent kinetics in catalyzing both oxygen evolution reaction (OER) and hydrogen evolution reaction (HER), which surpass the benchmark catalysts RuO₂ and Pt/C. The doping strategy is demonstrated to further enhance electrocatalytic performance by constructing Mo-doped Ni₂Si PMEC, which requires only a cell voltage of 1.60 V at 100 mA cm⁻². Density functional theory calculations display that the synergistic effect of Ni and Si can reduce the energy barriers of intermediate adsorption, and the introduction of Mo into Ni₂Si can further decrease the energy barrier of determining step and optimize the H^{*} adsorption energy, thus enhancing the electrochemical kinetics for OER and HER. Our work paves the way for designing high-efficiency and low-cost porous monolith catalysts through a facile and scalable method, showing great prospects for industrialization.

1. Introduction

Hydrogen, as an energy carrier, can be generated from water electrolysis using other renewable energies, which is crucial for the future of global carbon neutrality [1,2]. Water splitting, which includes the oxygen evolution reaction (OER) and the hydrogen evolution reaction (HER), is an attractive technology for hydrogen production due to low cost, large scale, and sustainability [3,4]. However, the OER and HER activities are limited because of their sluggish kinetics and large overpotentials, necessitating highly active electrocatalysts to overcome energy barriers [5–7]. At present, RuO₂/IrO₂ and Pt/Pd are the outstanding catalysts for OER and HER, respectively, but their scarcity and poor stability in alkaline media make them practical use undesirable [8,9]. Therefore, there is an urgent need to rationalize the design of noble metal-free electrocatalysts for water splitting with high activity, good durability, and large scale, but this remains a challenge.

Recently, transition metals (such as Co, Fe, Mo, and Ni), owing to their low price and adjustable intrinsic catalytic properties, have been

used as robust and highly efficient electrocatalysts for water splitting [10], such as oxides [11], sulfides [12], carbides [13], nitrides [14], phosphides [12,15] and hydroxides [16], etc. Among them, Ni-based electrocatalysts show good OER and HER activities and durability, making them an economical and efficient substitute for water splitting [17]. However, compared to noble metal-based catalysts, Ni-based ones still have room for improvement in water splitting performance. As a result, extensive efforts have been directed towards the preparation of Ni-based electrocatalysts to enhance the intrinsic activity [18]. Alloying with other transition metals and morphology engineering are the most used strategies to improve the catalytic activity [19]. Recent studies have shown that the catalysts combining elemental compositions with morphology engineering display excellent catalytic activity [20,21]. Additionally, the stability of electrodes for producing hydrogen is another important factor in practice. The electrodes are usually prepared by attaching catalysts to the conductive substrate (such as carbon fibers and three-dimensional metal supports) with a binder polymer (such as Nafion), but the supports are high cost and prone to corrosion,

* Corresponding author.

E-mail address: jiangyao@csu.edu.cn (Y. Jiang).

which will largely hamper their practical uses [10,22,23]. Therefore, developing a self-supporting electrocatalyst with high efficiency and long-term stability to avoid the above problems is of significant importance for industrial use.

At present, more attention has been paid to the investigation of non-precious metal complex catalysts [24–29]. Despite the high catalytic activity of many catalysts themselves, there still exist some drawbacks (such as sluggish reaction kinetics, restricted reaction sites, and poor conductivity) during application [30]. More notably, many catalysts are still in powder form that needs an extra current collector, and the powders are prone to fall off due to the weak adhesion [31]. In contrast, the substrate-free and binder-free monolithic catalyst can overcome these issues. Therefore, the non-precious metal complex catalysts with the monolithic structure merit further attention.

Transition metal silicides, owing to specific crystal structure and electronic structure, show high stability and conductivity which are important factors for water splitting [32]. However, their catalytic activity needs to be further improved. On the other hand, atom doping is considered an effective strategy to build new heterojunction structures combined not only with oxygen-containing intermediates but also with hydrogen-containing intermediates, which is in favor of enhancing the overall water splitting performances [25]. Therefore, we propose a long-range ordered nickel silicide combined with a doping strategy to obtain a promising candidate for water splitting. Strong coupling effects are generated between large numbers of heterogeneous interfaces by introducing the Mo element [25]. Moreover, 3D porous structure is beneficial for enhancing catalytic performance due to numerous exposed active sites [33]. Inspired by the above considerations, we report a scalable reactive synthesis method to fabricate Ni₂Si-based porous monolith electrocatalysts (PMECs) for overall water splitting in alkali. The as-prepared Ni₂Si PMECs exhibit good OER, HER, and overall water splitting performances, which outperform the benchmarks and many recently reported catalysts. The Mo-doped Ni₂Si (Mo: Ni₂Si = 20: 100) PMEC exhibits superior electrocatalytic activity and good long-term stability, achieving the overpotentials of 287 mV for OER and 194 mV for HER, and a cell voltage of 1.60 V for overall water splitting at 100 mA cm⁻², respectively, which ranks among the top of the recently reported electrocatalysts. The strong synergistic effect between Ni, Si, and Mo can significantly optimize the adsorption free energies of intermediates to enhance OER and HER activities. This work offers a simple and scalable way for developing porous monolith electrocatalysts, shedding new light on practical applications for overall water splitting.

2. Experimental methods

2.1. Electrocatalysts preparation

The Ni₂Si PMEC was fabricated via a reactive synthesis method. Initially, the stoichiometric quantities of Ni (D₅₀ = 33.1 μm, 99.9%) and Si (D₅₀ = 13.2 μm, 99.9%) elemental powders were mixed on a V-type mixer for 48 h. Subsequently, the mixed powders were pressed into the green compacts with sizes of 60 × 10 × 2.5 mm and Φ30 × 3 mm through the uniaxial pressure of 100 MPa for 10 s. Following this, a quartz boat was placed in the heating zone, filled with the green compacts. The furnace was heated at 5°C/min to 700°C and held there for 210 min in a vacuum. After reaching 700°C, the heating rate of the vacuum furnace was carried out at 1°C/min, which is important to obtain the Ni₂Si phase. The vacuum furnace was heated to 750°C, 800°C, and 850°C for 120 min each, and the heater was turned off. Natural cooling to room temperature ends the sintered process.

The procedure to prepare Mo-doped Ni₂Si PMECs was the same as that of Ni₂Si PMEC, except that Mo elemental powder (D₅₀ = 9.88 μm, 99.9%) was used. In order to find the optimal amount of Mo doping for Ni₂Si, various amounts of Mo elemental powder (Mo: Ni₂Si = 5: 100, 10: 100, 15: 100, 20: 100, and 30: 100, denoted as Mo-Ni₂Si-5, Mo-Ni₂Si-10,

Mo-Ni₂Si-15, Mo-Ni₂Si-20, and Mo-Ni₂Si-30, respectively) were added into the mixed Ni₂Si powders.

2.2. Material characterizations

X-ray diffraction (XRD, Bruker D8 Advance) measurements were performed to investigate the phases of the porous catalysts. Scanning electron microscopy (SEM, TESCAN/MIRA 3) measurements were acquired to investigate the morphologies of the porous catalysts before and after stability tests. Transmission electron microscopy (TEM) measurements were performed by JEM-F200, and the TEM samples were prepared by focused ion beam (FIB). The compositions of porous catalysts were determined using inductively coupled plasma-optical emission spectroscopy (ICP-OES, iCAP7600) and chemical analysis. X-ray photoelectron spectroscopy (XPS, ESCALABSB 250 Xi) measurements were carried out to analyze the elemental valence of porous catalysts, and all binding energies were calibrated for sample charging by aligning C 1 s peak at 284.8 eV. The specific surface area measurement was performed by nitrogen adsorption at 77 K (Quadasorb SI-3MP). The open porosities of porous samples were determined by the Archimedes method. The electrical conductivity for Ni₂Si-based PMECs was obtained using a four-probe tester (ST-2258 C) under an air atmosphere.

2.3. Electrochemical measurements

The electrochemical measurements were carried out in 1 M KOH electrolyte, in which the platinum foil and Hg/HgO electrode were utilized as the counter and reference electrodes, respectively, in a three-electrode system using an electrochemical workstation (CHI660D). The Ni₂Si-based PMECs were used as the working electrodes with an electrode area of 1 cm². For comparison, catalyst ink including commercial 20% Pt/C or RuO₂ powder was prepared by dispersing 5 mg of the catalyst in a mixture of water (750 μL), ethanol (250 μL), and 5% Nafion (30 μL) solution, followed by ultrasound for 30 min. Then the Pt/C and RuO₂ electrodes were prepared by dropping 10 μL of the catalyst inks on a glass carbon electrode with an area of 0.071 cm² for HER and OER tests, respectively. Before the measurement, several cyclic voltammetry (CV) scans were applied to electrochemically activate the as-prepared electrodes to reach a stable state. The linear sweep voltammetry (LSV) curves were recorded at a scan rate of 1 mV s⁻¹. The Tafel slope can be derived from the polarization curve and used to judge the reaction kinetics of materials. All potentials reported in this work were transferred to the reversible hydrogen electrode (RHE) potentials using the Nernst equation: $E_{RHE} = E_{Hg/HgO} + 0.059 \text{ pH} + 0.098 \cdot iR_s$, where $E_{Hg/HgO}$ is the measured potential, i is the measured current, R_s is the uncompensated resistance. All LSV curves for OER and HER were background corrected. To assess the double-layer capacitance (C_{dl}), CV curves were carried out at different scanning rates (50, 60, 70, 80, 90, and 100 mV s⁻¹) in the non-Faradic region. The corresponding electrochemically active surface area (ECSA) can be evaluated by C_{dl} values. The CV curves (100 mV s⁻¹) and chronopotentiometry curves (100 mA cm⁻² without iR correction) were performed to investigate the stability performances. Overall water splitting performances were carried out using a two-electrode configuration consisting of the as-prepared electrocatalysts as both anode and cathode. Commercial RuO₂ and 20% Pt/C catalysts were used as references by dropping the catalyst inks on the Ni foam for overall water splitting. The Faradaic efficiency was determined by comparing the measured amount of evolved gas with the calculated amount of gas.

3. Results and discussion

3.1. PMECs fabrication and structure characterization

The fabrication approach of Ni₂Si PMEC using a simple reactive synthesis method is schematically depicted in Fig. 1a. First, the Ni and Si elemental powders were mixed evenly, followed by cold pressing to

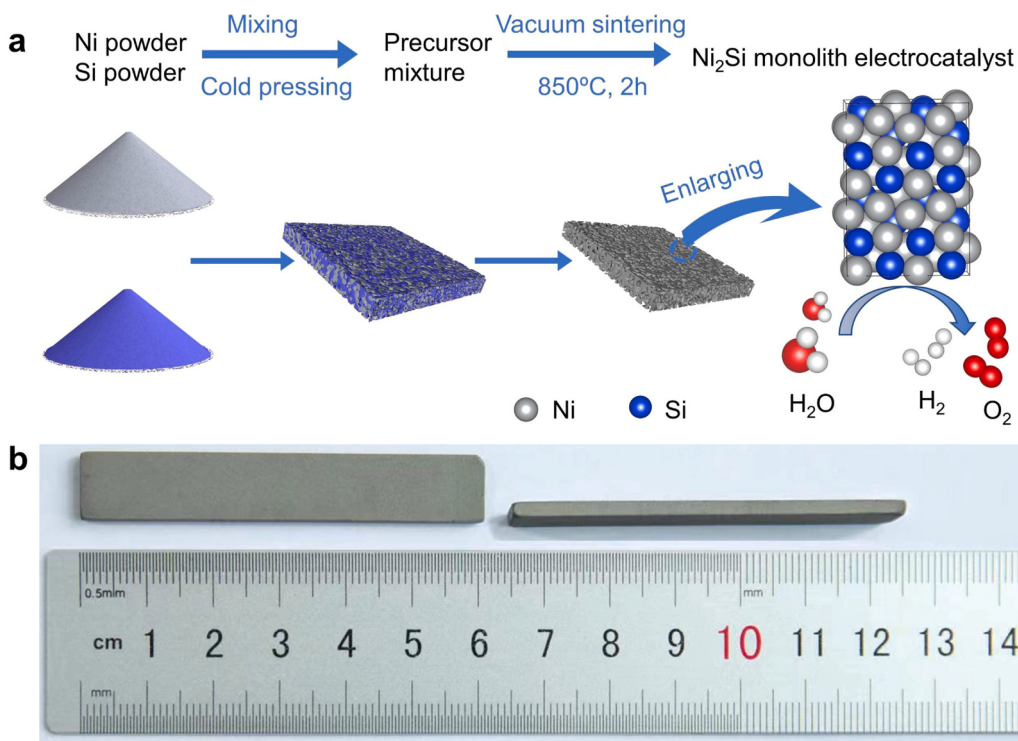


Fig. 1. Fabrication of PMECs using reactive synthesis method. (a) Schematic representation of the preparation procedure. (b) Photograph.

obtain a thin cuboid precursor mixture and vacuum sintering to produce the Ni₂Si PMEC. The Mo-doped Ni₂Si PMECs were also fabricated via the same process with the introduction of Mo elemental powder. The production of PMECs can be easily scaled up, and the size of PMEC is limited by the size of the mold (Fig. 1b). Recently, commonly used methods for preparing catalysts, such as electro-deposition and hydrothermal approach, often entail strict reaction conditions and toxic waste production, being difficult to prepare on a large scale [34–36]. Compared to those methods, the reactive synthesis method is a facile and scalable approach to produce this class of multifunctional materials.

To verify that the Ni₂Si PMEC is successfully synthesized, XRD is used to analyze the crystalline structure (Fig. 2a). The XRD peaks match well with the orthorhombic Ni₂Si (PDF#97-016-5257), suggesting the high purity of PMEC. The SEM images (Fig. 2b) exhibit that the Ni₂Si PMEC is free-standing with numerous micro-sized pores, suggesting a high surface area for the efficient realization of the exchange of proton or intermediates including oxygen [37]. The elemental mapping patterns of the Ni₂Si PMEC clearly exhibit the even distributions of Ni and Si elements (Fig. S1). Furthermore, the ICP-OES, chemical analysis, and energy-dispersive X-ray (EDX) confirm the stoichiometry of Ni₂Si, and the weight ratios of Ni and Si from SEM-EDX result are basically close to those of ICP-OES and chemical analysis (Table S1). Additionally, the Ni₂Si PMEC shows a large open porosity value of 54%, and the corresponding specific surface area is 0.274 m² g⁻¹ (Fig. S2 and S3). The selected area electron-diffraction (SAED) pattern of Ni₂Si identifies the exposed (001), (011), and (010) crystal planes of Ni₂Si along the [100] zone axis (Fig. 2c). The HRTEM image indicates the lattice fringes with interplanar distances of ~0.329 nm that corresponds to the (011) plane of Ni₂Si (Fig. 2d), in agreement with the XRD result. The TEM-EDX result shows the Ni and Si signals in Ni₂Si. The elemental mapping images indicate that the Ni and Si elements are uniformly distributed and the corresponding weight ratio of Ni and Si is 87.37: 12.63, which is similar to the SEM-EDX result (86.76: 13.24) (Fig. 2e and Fig. S4). In addition, the surface compositions of Ni₂Si PMEC are measured by XPS (Fig. 2f-h). More specifically, the XPS survey spectra of Ni₂Si PMEC confirm the presence of Ni and Si elements (Fig. 2f). For the high-resolution Ni 2p

spectrum (Fig. 2g), the peaks at 852.96, 870.17, 856.02 and 874.06 eV correspond to Ni⁰ 2p_{3/2}, Ni⁰ 2p_{1/2}, Ni²⁺ 2p_{3/2} and Ni²⁺ 2p_{1/2}, respectively [38]. Two satellite peaks of Ni 2p appear at 861.31 and 879.96 eV. The Si 2p spectrum (Fig. 2h) displays the existence of Si⁰ (99.49 and 100.17 eV for Si⁰ 2p_{3/2} and Si⁰ 2p_{1/2}, respectively), and a peak at 102.84 eV corresponds to SiO_x [39,40]. These results indicate that the low valence and high valence of elements coexist in the Ni₂Si PMEC, which are favorable for electro-reduction and electro-oxidation reactions [41–43].

3.2. Electrochemical performance of Ni₂Si PMECs

To evaluate the electrocatalytic activity, the OER and HER performances of Ni₂Si PMECs were investigated with a standard three-electrode configuration in 1 M KOH. In detail, as shown in Fig. 3a, the Ni₂Si PMEC shows low OER overpotentials of 273, 332, and 353 mV at 10, 50, and 100 mA cm⁻², respectively. The anodic peak appears at around 1.4 V on the polarization curves of the Ni₂Si PMEC, which is related to the Ni²⁺/Ni³⁺ oxidation peak [44]. Moreover, the Ni₂Si PMEC shows a lower Tafel slope compared to RuO₂, indicating the faster reaction kinetics on the Ni₂Si PMEC for OER (Fig. 3b). To further analyze the OER performance of different catalysts, the overpotentials at 10 mA cm⁻² and the Tafel slopes are summarized. This performance surpasses that of RuO₂ ($\eta_{10} = 306$ mV) and many recently reported OER electrocatalysts (Fig. 3c and Table S2). The HER performance of the Ni₂Si PMEC was evaluated by polarization curves, with Pt/C as the reference (Fig. 3d). The overpotentials for the Ni₂Si PMEC are 80, 200, and 261 mV at 10, 50, and 100 mA cm⁻², respectively, which are lower than that of Pt/C at larger current densities (> 150 mA cm⁻²) and most reported HER electrocatalysts at 10 mA cm⁻² (Table S3). In addition, the Ni₂Si PMEC shows a comparable Tafel slope to that of Pt/C, further indicating the favorable HER kinetics (Fig. 3e, f).

Apart from the OER and HER performances, electrochemical stability is another important factor for judging a promising electrocatalyst. Chronopotentiometry and cyclic voltammetry tests for OER and HER were performed to investigate the stability of the Ni₂Si PMEC (Fig. 3g-i).

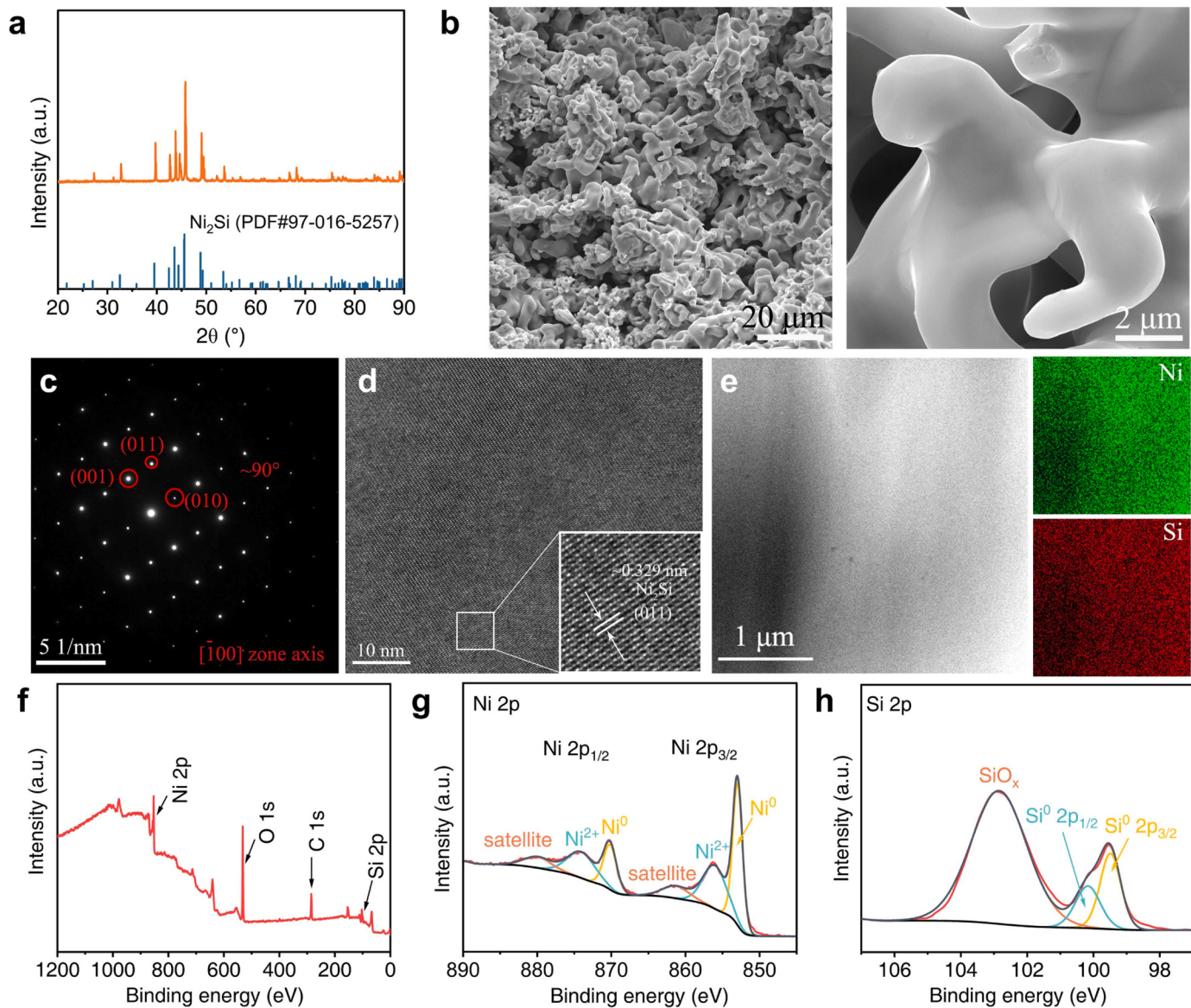


Fig. 2. Characterization of Ni₂Si PMECs. (a) XRD pattern of Ni₂Si. (b) SEM images of Ni₂Si. (c) SAED pattern. (d) HRTEM image. (e) TEM image and EDX elemental mapping. (f) XPS survey of Ni₂Si, and (g, h) high-resolution XPS of (g) Ni 2p and (h) Si 2p.

The chronopotentiometry curves of the Ni₂Si PMEC for OER and HER display no obvious degradation of potential after testing for 100 h at the large current density of 100 mA cm⁻², demonstrating significantly better stability than that of RuO₂ and Pt/C, respectively (Fig. 3g and Figs. S5 and S6). Moreover, the structure and morphology of the Ni₂Si PMEC were demonstrated by XRD, SEM, and XPS analysis after 100 h at 100 mA cm⁻² for OER and HER (Figs. S7-S9), and the Ni₂Si PMEC can well remain the initial composition and porous morphology. In addition, the OER polarization curve of the Ni₂Si PMEC has a slight left shift (~28.8 mV negative shift of overpotential at 100 mA cm⁻²) and exhibits significantly higher catalytic activity after 5000 cycles than that of the initial curve, which may be attributed to the significant decreases in the Ni⁰/Ni²⁺ ratio during anodic oxidation. The potential of the polarization curve after 10000 cycles is reduced compared with the potential after 5000 cycles but shows small changes in contrast to that of the initial curve, and the HER polarization curves almost overlap before and after 5000 cycles, suggesting excellent stability of the Ni₂Si PMEC (Fig. 3h, i).

Considering that the Ni₂Si PMEC has outstanding catalytic activity and stability, we rationally assembled a two-electrode system by using the Ni₂Si PMECs as both anode and cathode toward alkaline overall

water splitting to explore practical use. The Ni₂Si PMEC||Ni₂Si PMEC couple exhibits promising overall water splitting activity, and the cell voltages to deliver current densities of 10, 50, and 100 mA cm⁻² are 1.60, 1.77, and 1.83 V, respectively, which is superior to RuO₂||Pt/C and most reported bifunctional catalysts (Fig. 3j and Table S4). Regarding their long-term stability, it is noted that negligible degradation of the Ni₂Si PMECs for over 100 h at a large current density of 100 mA cm⁻² is observed, while the voltage of RuO₂||Pt/C increases significantly, indicating good long-term stability (Fig. 3k). Besides, the composition and porous morphology of the Ni₂Si PMEC after the stability test maintain unchanged (Figs. S10 and S11). Numerous bubbles were continuously produced at the Ni₂Si PMEC||Ni₂Si PMEC couple, indicating that the bubbles do not accumulate in large quantities and can effectively dispatch from the smooth surface of the electrocatalysts (Fig. 3l). Furthermore, the measured amount of H₂ and O₂ is close to the calculated amount, and the Faradaic efficiency of Ni₂Si catalysts can reach up to 98% (Fig. S12). In addition to the electrochemical performance, the earth abundance, cost-efficacy, robustness, and scalability of the Ni₂Si PMEC are other significant advantages for its large-scale industrial utilization.

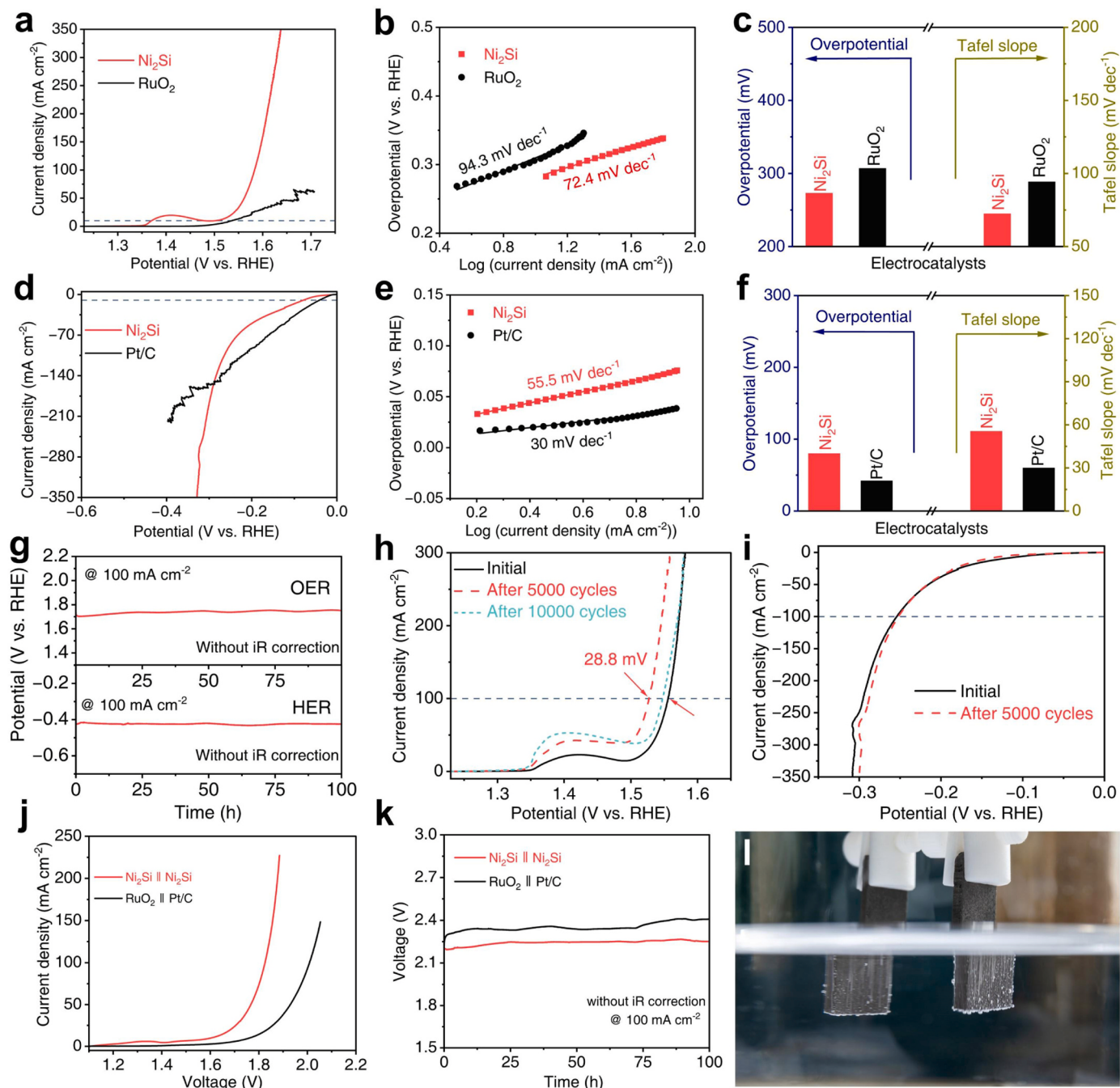


Fig. 3. Electrochemical performance of Ni_2Si PMEC in 1 M KOH. (a) OER polarization curves. (b) Tafel curves. (c) Histogram for overpotentials at 10 mA cm^{-2} and Tafel slopes. (d) HER polarization curves. (e) Tafel curves. (f) Histogram for overpotentials at 10 mA cm^{-2} and Tafel slopes. (g) Chronopotentiometry curves of Ni_2Si PMEC for OER and HER at 100 mA cm^{-2} . (h, i) polarization curves with different CV cycles for (h) OER polarization curves and (i) HER polarization curves. (j) Polarization curves of Ni_2Si PMEC|| Ni_2Si PMEC and $\text{RuO}_2||\text{Pt/C}$ at a scan rate of 1 mV s^{-1} . (k) Chronopotentiometry curves of Ni_2Si PMEC|| Ni_2Si PMEC and $\text{RuO}_2||\text{Pt/C}$ at 100 mA cm^{-2} . (l) Photo image of the gas bubble.

3.3. Density functional theory (DFT) calculation

To further understand the origins of the excellent electrocatalytic activity of Ni_2Si for OER and HER, DFT models of Ni_2Si and pure Ni were constructed to obtain the free energy values of every stage (Figs. S13–S17). According to the XRD results, the (013) plane of Ni_2Si was calculated to explain the intrinsic mechanism (Fig. 4). The free energy values of Ni_2Si and pure Ni for OER are shown in Fig. 4a and Figs. S13–S15. The rate-determining steps of Ni_2Si on Ni and Si sites, and pure Ni appear at the transition from ${}^*\text{O}$ to ${}^*\text{OOH}$. The lower energy barrier (3.41 eV) on the Ni sites of Ni_2Si compares with that of 3.43 eV on the Si

sites of Ni_2Si , suggesting that the Ni sites of Ni_2Si are the active sites. In contrast, the free energy value of pure Ni (111) is 3.78 eV, which is larger than that of Ni_2Si , revealing the poorer OER performance of pure Ni than that of Ni_2Si . The reduced free energy of ${}^*\text{OOH}$ can promote the ${}^*\text{OOH}$ formation, which facilitates reaction kinetics and catalytic capacity for OER [45]. In addition, the OER mechanisms for Ni_2Si are investigated, and the corresponding four stages are displayed in Fig. 4b. The Gibbs free energy of the adsorbed intermediate (ΔG_{H^*}) is a major descriptor to evaluate the HER performance, and the optimum ΔG_{H^*} value should be close to zero [46,47]. There are three active sites of Ni_2Si labeled as site 1 (Ni-Ni-Si bridge), site 2 (Ni-Ni-Ni bridge), and site

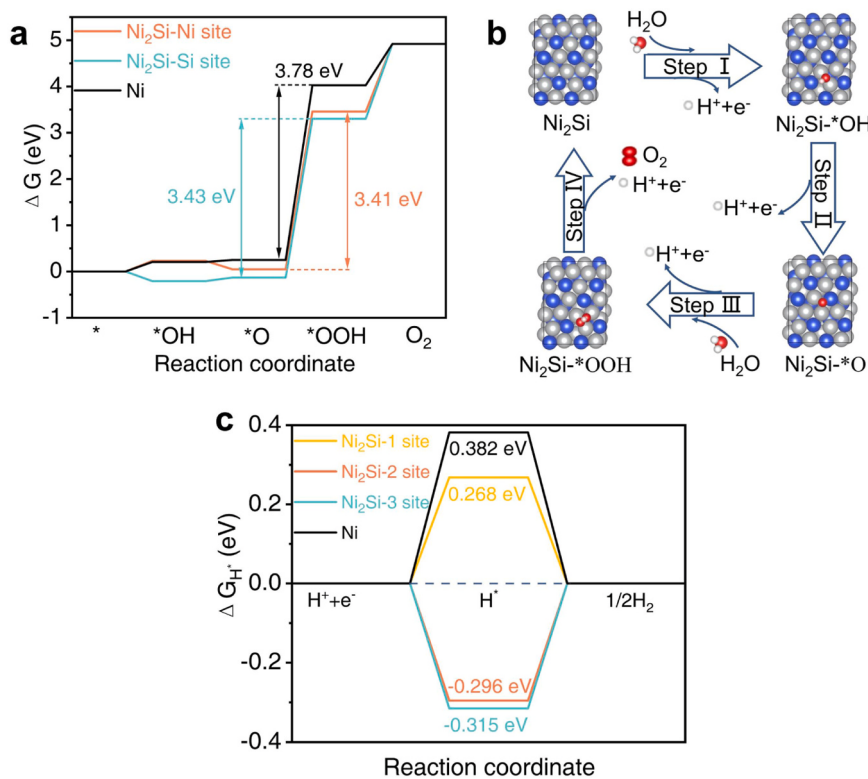


Fig. 4. Theoretical calculations. (a) Free energy diagram of OER for Ni_2Si and Ni. (b) Proposed OER pathway on Ni sites of Ni_2Si . (c) Free energy diagram of HER for Ni_2Si and Ni.

3 (Ni-Ni-Ni bridge) in Fig. S16. The ΔG_{H^*} of site 1 is 0.268 eV, which is closer to zero than that of site 2 (−0.296 eV) and site 3 (−0.315 eV), indicating the optimal H^* adsorption kinetics on site 1 (Fig. 4c). The ΔG_{H^*} value of pure Ni (111) is 0.382 eV, suggesting the weak adsorption of H^* (Fig. 4c and Fig. S17). Consequently, the synergistic effect between Ni and Si can decrease the energy barriers of intermediate adsorption, leading to the promotion of OER and HER electrocatalysis.

3.4. Electrochemical performance of Mo-doped Ni_2Si PMECs

To further improve electrocatalytic performance, parameters for a catalyst, such as composition, doping, and morphology, need to be rationally designed to maximize the number of active sites and ensure fast electron transport [48–51]. Composition and doping are effective strategies for improving electrocatalytic activity. Among them, the addition of transition metals, such as Fe and Mo, can change the electronic state and rearrange the valence electrons [52–54]. Regarding morphology engineering, Raney Ni is the industrially used electrocatalyst, which possesses a large surface area, low price, and good stability, but its complex preparation process and poor catalytic activity make its electrocatalytic performance unsatisfactory [55,56]. In addition, when applying larger current densities, evolved bubbles covering the catalyst surface are also an important problem for industrial water electrolysis. To solve the above problems, combining the 3D porous structure and doping is expected to obtain more active sites and better catalytic performance for water splitting. Thus, the Mo-doped Ni_2Si -based PMECs were systematically investigated.

The electrocatalytic activities of Mo-doped Ni_2Si PMECs toward OER and HER are investigated. The XRD, SEM, and open porosity results of Mo-doped Ni_2Si PMECs demonstrate the formation of the main Ni_2Si phase with porous structure (Fig. S2a and Figs. S18 and S19). The compositions of Mo-doped Ni_2Si PMECs were determined by ICP-OES, chemical analysis, and SEM-EDX, which confirm the stoichiometry of Mo-doped Ni_2Si , indicating that the composition of Ni_2Si is well

maintained (Fig. S20 and Table S1). The porous structure of Mo-doped Ni_2Si PMECs was further analyzed using nitrogen adsorption-desorption method (Fig. S21). At low relative pressures, the isotherm loops of all Mo-doped PMECs show irreversible sorption profiles, suggesting typical microporous character [57]. The specific surface area of the Mo- Ni_2Si -20 ($0.34 \text{ m}^2 \text{ g}^{-1}$) is higher than that of Mo- Ni_2Si -5 ($0.18 \text{ m}^2 \text{ g}^{-1}$), Mo- Ni_2Si -10 ($0.20 \text{ m}^2 \text{ g}^{-1}$), and Mo- Ni_2Si -15 ($0.22 \text{ m}^2 \text{ g}^{-1}$), and the corresponding trend in change is consistent with open porosity. The SAED pattern and HRTEM image of Mo- Ni_2Si -20 are well indexed to the Ni_2Si structure, and the EDX results show the even distribution of elements (Fig. S22). The polarization curves for OER of Mo-doped Ni_2Si PMECs and the corresponding overpotentials at different current densities are displayed in Fig. 5a, d and Fig. S23. The Mo- Ni_2Si -20 needs the lowest overpotentials of 142 and 287 mV to achieve 10 and 100 mA cm^{-2} , respectively, as displayed for Ni_2Si (273 and 353 mV), Mo- Ni_2Si -5 (227 and 322 mV), Mo- Ni_2Si -10 (186 and 311 mV), and Mo- Ni_2Si -15 (161 and 291 mV). The incorporation of Mo can significantly improve the catalytic performance. This may be attributed to the increased concentration of doped Mo in Ni_2Si as the Mo dopant concentration increases, as demonstrated by the leftward shift of the XRD peaks (Fig. S18b). Moreover, Mo- Ni_2Si -20 shows the lowest Tafel slope among Ni_2Si , Mo- Ni_2Si -5, Mo- Ni_2Si -10, and Mo- Ni_2Si -15, indicating the fastest OER kinetics of Mo- Ni_2Si -20 (Fig. S24). To characterize the kinetics of the catalyst, electrochemical impedance spectroscopy (EIS) measurements were carried out. The charge-transfer resistances (R_{ct}) are associated with the reactant adsorption and production desorption. Since the ohmic resistance (R_{s}) of catalysts is similar, the smaller R_{ct} will result in better mass transfer [58]. The R_{ct} value of Mo- Ni_2Si -20 ($\sim 2.1 \Omega$) is smaller than those of Ni_2Si ($\sim 4.2 \Omega$), Mo- Ni_2Si -5 ($\sim 3.1 \Omega$), Mo- Ni_2Si -10 ($\sim 2.8 \Omega$), and Mo- Ni_2Si -15 ($\sim 2.3 \Omega$), demonstrating the fastest reaction kinetics of Mo- Ni_2Si -20 in OER (Fig. S25). As shown in Fig. 5b, e, the Mo- Ni_2Si -20 shows the best HER performance with low overpotentials of 53 and 194 mV to achieve 10 and 100 mA cm^{-2} , respectively, as displayed for Ni_2Si (80 and

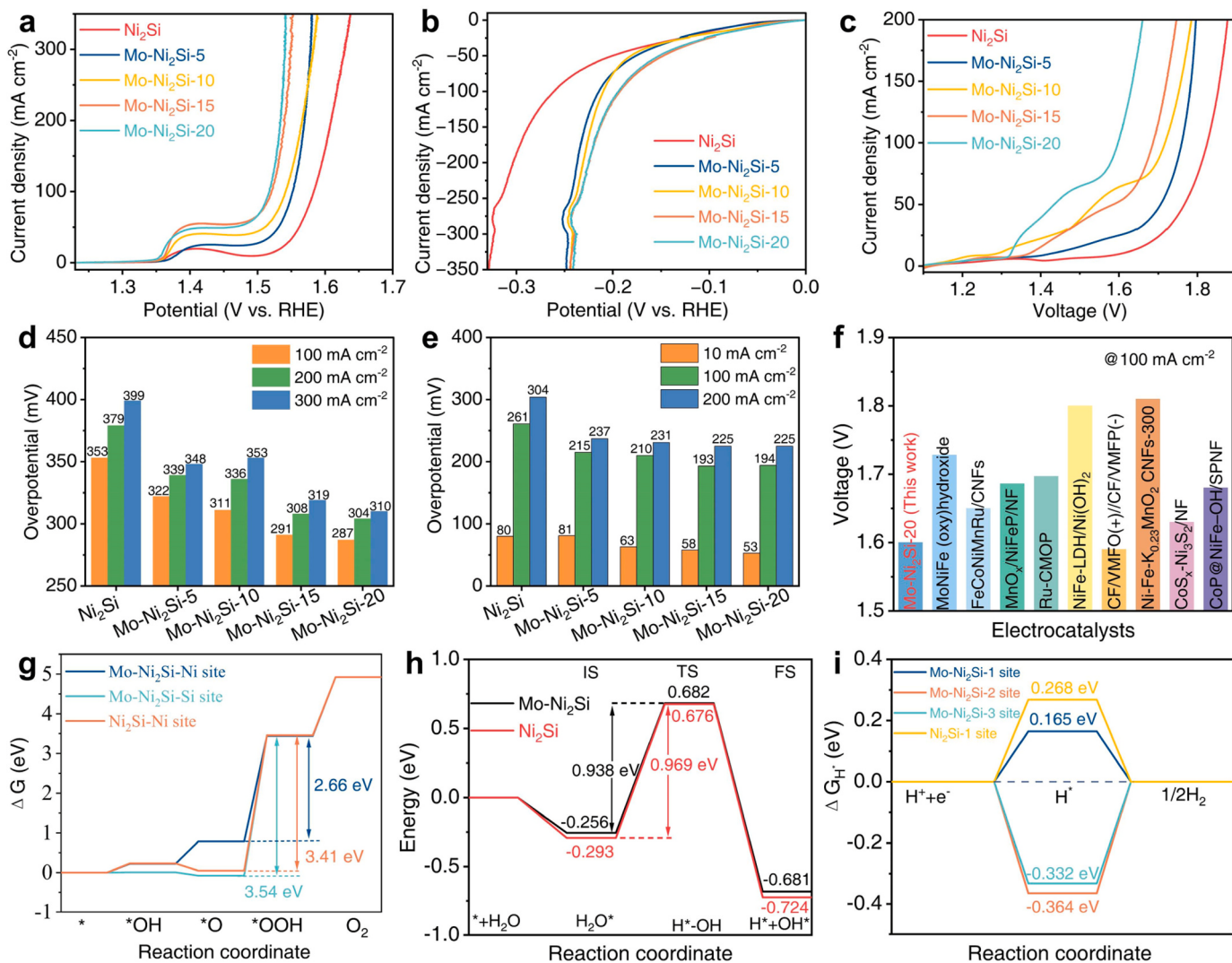


Fig. 5. Electrochemical performance and DFT calculations of Mo-doped Ni₂Si PMECs. (a) Polarization curves for OER. (b) Polarization curves for HER. (c) Polarization curves for overall water splitting. (d, e) overpotentials at different current densities of (d) OER and (e) HER. (f) Comparison of voltage of Mo-Ni₂Si-20 at 100 mA cm⁻². (g) Free energy diagrams of Ni₂Si and Mo-doped Ni₂Si for OER. (h) Energy barriers for water dissociation processes of Ni₂Si and Mo-doped Ni₂Si. The IS, TS, and FS are the initial state, transition state, and final state, respectively. (i) The calculated ΔG_{H^*} of Ni₂Si and Mo-doped Ni₂Si.

261 mV), Mo-Ni₂Si-5 (81 and 215 mV), Mo-Ni₂Si-10 (63 and 210 mV), and Mo-Ni₂Si-15 (58 and 193 mV). The smallest Tafel slope of Mo-Ni₂Si-20 is 36.8 mV dec⁻¹, obviously superior to that of Ni₂Si (55.5 mV dec⁻¹), Mo-Ni₂Si-5 (61.3 mV dec⁻¹), Mo-Ni₂Si-10 (56.1 mV dec⁻¹), and Mo-Ni₂Si-15 (51.8 mV dec⁻¹), indicating that the kinetics of Mo-Ni₂Si-20 are fastest during hydrogen production (Fig. S26). The R_{ct} value of Mo-Ni₂Si-20 is about $\sim 1.9 \Omega$, which is smaller than Ni₂Si ($\sim 25.5 \Omega$), Mo-Ni₂Si-5 ($\sim 6.9 \Omega$), Mo-Ni₂Si-10 ($\sim 4.7 \Omega$), and Mo-Ni₂Si-15 ($\sim 2.1 \Omega$), indicating the faster electron transfer of Mo-Ni₂Si-20 in HER (Fig. S27). The electrocatalytic performances of Mo-Ni₂Si-30 are presented in Fig. S28. The OER and HER overpotentials of Mo-Ni₂Si-30 to acquire 100 mA cm⁻² are 292 and 199 mV, respectively, which are slightly higher than those of Mo-Ni₂Si-20. The EIS results show that the Mo-Ni₂Si-30 results in sluggish electron transport capability for both OER and HER. Therefore, the Mo-Ni₂Si-20 exhibits the best electrocatalytic activity toward OER and HER. To further understand the enhanced activity of Mo-doped Ni₂Si PMECs, the electrochemical double-layer capacitances (C_{dl}) were measured, which is in direct proportion to the electrochemically active surface area (ECSA). The C_{dl} of Mo-Ni₂Si-20 is 17.07 mF cm⁻², clearly larger than that of Ni₂Si (8.64 mF cm⁻²), Mo-Ni₂Si-5 (11.52 mF cm⁻²), Mo-Ni₂Si-10 (15.96 mF cm⁻²), and Mo-Ni₂Si-15 (15.79 mF cm⁻²), implying that the porous structure and

Mo doping offer a larger activity surface area (Figs. S29-S31). The large ECSA suggests that the catalytic reactions possess abundant active sites, being beneficial to water molecule adsorption and intimate contact with the electrolyte, which can account for enhanced electrochemical activity [59].

The Mo-Ni₂Si-20 maintains stable OER and HER activities over 100 h at 100 mA cm⁻², indicating good long-term durability at the large current density (Figs. S32 and S33). After stability tests, the composition and morphology are analyzed using XRD, SEM, and XPS (Figs. S34-S36). The XRD and SEM results display an unchanged composition and a similar morphology. The Ni 2p spectra show the existence of Ni⁰ and Ni²⁺, and the Si 2p spectra suggest the presence of Si⁰ and SiO_x. In the Mo 3d spectra of as-prepared Mo-Ni₂Si-20, peaks at 227.82, 230.96, 228.98, 232.40, and 235.50 eV are assigned to Mo⁰ 3d_{5/2}, Mo⁰ 3d_{3/2}, Mo⁴⁺ 3d_{5/2}, Mo⁴⁺ 3d_{3/2}, and Mo⁶⁺ 3d_{3/2}, respectively [60]. After the OER stability test, the low valence of Ni, Si, and Mo elements disappear and the high valence of all elements notably increases due to a highly oxidative environment. After the HER stability test, the XPS spectra of Mo-Ni₂Si-20 indicate that the change in chemical compositions is unobvious. The high OER and HER stabilities of Mo-Ni₂Si-20 are confirmed by chronopotentiometry and EIS curves (Fig. S37). The negligible potential and resistance changes demonstrate the

electrocatalytic stability of Mo-Ni₂Si-20. In addition, the polarization curves of Mo-Ni₂Si-20 show negligible change after 5000 cycles at high current density ($> 100 \text{ mA cm}^{-2}$) except for a slight shift for the Ni²⁺/Ni³⁺ oxidation peak, indicating good cycling stability toward OER (Fig. S38a). The phase and morphology are characterized by XRD and SEM after cycling stability, and there is no obvious change in the phase and morphology of Mo-Ni₂Si-20, further confirming high structural stability (Fig. S38b-d). Meanwhile, the Faradaic efficiencies of O₂ and H₂ are about 99.7% and 98.5%, respectively, indicating low electron loss of Mo-Ni₂Si-20 during the energy conversion process (Fig. S39).

The Mo-doped Ni₂Si PMECs were used as both anode and cathode to construct a two-electrode system for overall water splitting. The cell voltages of Mo-Ni₂Si-20 at 10 and 100 mA cm⁻² are 1.42 and 1.60 V, respectively, as displayed for Ni₂Si (1.60 and 1.83 V), Mo-Ni₂Si-5 (1.51 and 1.76 V), Mo-Ni₂Si-10 (1.45 and 1.72 V), and Mo-Ni₂Si-15 (1.43 and 1.69 V) (Fig. 5c and Fig. S40a). The cell voltage of Mo-Ni₂Si-30 is higher than Mo-Ni₂Si-20 due to its poorer HER and OER catalytic activities (Fig. S40b). The water-splitting performance of Mo-Ni₂Si-20 ranks among the top of the many recently reported electrocatalysts, making it extremely promising for practical use (Fig. 5f and Table S5). Meanwhile, the Mo-Ni₂Si-20 as bifunctional electrodes show good long-term durability at the large current density of 100 mA cm⁻² for 100 h (Fig. S41). Furthermore, the structural and morphologic changes of Mo-Ni₂Si-20 are characterized by XRD and SEM after the overall water splitting test, which show a similar phase composition and morphology (Figs. S34 and S42). In addition to the superior catalytic activity of catalysts themselves, the high electrical conductivity of catalysts is also conducive to efficient electrocatalysis [61]. The electrical conductivity of Mo-doped Ni₂Si PMECs was performed to explore their charge transfer ability (Fig. S43). At room temperature, the electrical conductivities for Ni₂Si, Mo-Ni₂Si-5, Mo-Ni₂Si-10, Mo-Ni₂Si-15, and Mo-Ni₂Si-20 are 4.24×10^5 , 4.29×10^5 , 3.46×10^5 , 3.44×10^5 , and $2.11 \times 10^5 \text{ S m}^{-1}$, respectively. The conductivities of Mo-doped Ni₂Si reduce with an increase in Mo dopant concentration, which may be related to the increased electron scattering effect at the interfaces to reduce the electrical conductivity [62]. The conductivities of Mo-doped Ni₂Si PMECs are larger than those of Ta₂CS₂ ($3.149 \times 10^4 \text{ S m}^{-1}$) [63], graphite ($1.3 \times 10^5 \text{ S m}^{-1}$) [64], MoS₂ (547 S m^{-1}) [65], and CaMnO₃ ($3.33 \times 10^{-3} \text{ S m}^{-1}$) [66], suggesting the faster charge transfer kinetics. High electrical conductivity is favorable for improving overall performance, owing to minimizing ohmic losses and increasing active sites [67].

DFT calculations were carried out to offer deeper insights into the effect of Mo doping. The free energy values of Mo-doped Ni₂Si for OER were calculated and the corresponding models of Mo-doped Ni₂Si (Ni sites and Si sites) are displayed (Fig. 5g and Figs. S44 and S45). The rate-determining step of Mo-doped Ni₂Si appears at the generation of *OOH. The free energy value of 2.66 eV is obtained on the Ni sites, clearly lower than that of the Si sites (3.54 eV), indicating that the adsorption of intermediates on the Ni sites can decrease the energy barrier of OER. Compared to the Ni sites of Ni₂Si, the free energy value of the Ni sites of Mo-doped Ni₂Si is lower, which indicates that the enhancement of OER activity can be attributed to the doping of Mo. In the alkaline electrolyte, the rate of water dissociation is slow, which has greatly hindered the H₂ generation and the reaction kinetics [68]. Thus, the water dissociation energy barrier plays a significant role in determining the HER kinetic rate. The water dissociation energies were calculated and the corresponding atomic configurations were exhibited (Fig. 5h and Fig. S46). As a result, the downward water adsorption energies of Mo-doped Ni₂Si and Ni₂Si indicate that the water adsorption is thermodynamically favorable. The water dissociation energy barrier of Mo-doped Ni₂Si (0.938 eV) is smaller than that of Ni₂Si (0.969 eV), which effectively prompts the HO-H cleavage in water and results in rapid proton supply and alkaline HER kinetics [69]. Moreover, the ΔG_{H^*} values of Mo-doped Ni₂Si were calculated as displayed in Fig. 5i and Fig. S47. The ΔG_{H^*} value of site 1 (Ni-Mo-Si bridge) is 0.165 eV, clearly outperforming site 2 (Ni-Mo-Ni bridge) (-0.364 eV) and site 3 (Ni-Ni-Ni bridge)

(-0.332 eV), indicating that the H atom is easier to adsorb on site 1. Compared to site 1 of Ni₂Si, site 1 of Mo-doped Ni₂Si exhibits better catalytic kinetics, revealing that Mo doping can change the optimal active site. To further clarify the advantage of the doping of Mo for HER, the charge density difference analyses were performed (Fig. S48). After Mo doping, more electrons accumulate around the Mo atom (red dash line circle), which is conducive to optimizing the adsorption energy of H^{*} and thus improves HER activity. It should be noted that the theoretical overpotential should not be directly compared with the experimental overpotentials, as the theoretical models cannot be completely consistent with the realistic experimental conditions [70,71]. Additionally, the experimental value represents the potential-scale measure of activity, while the theoretical value represents the function of the current density [72]. Nonetheless, it is indicated that the change trends of Ni₂Si-based catalysts in theoretical overpotential are in good qualitative agreement with the ones in experimental results. In general, the doping of Mo can cause the strong synergistic effect between Ni, Si, and Mo, which can significantly optimize the free energies of adsorbed intermediates to enhance OER and HER activities.

4. Conclusions

In summary, a facile reactive synthesis method was reported to prepare Ni₂Si-based PMECs as highly efficient and robust bifunctional electrocatalysts. The Ni₂Si PMECs not only display superior OER and HER performances and good long-term durability but also exhibit promising catalytic activity for overall water splitting. After the introduction of Mo, the strong synergistic effect between Ni, Si, and Mo can significantly optimize the adsorption free energies of intermediates to enhance OER and HER activities. The Mo-doped Ni₂Si PMECs own exceptional electrocatalytic activity of catalysts themselves and high electrical conductivity, thus improving the overall performances. This work provides a new strategy to prepare PMECs with good long-term durability and high catalytic activity, which can be generalized to other materials to solve problems in practical applications.

CRediT authorship contribution statement

Zhenli He: Methodology, Investigation, validation, Writing – original draft, Writing – review & editing. **Yuehui He:** Conceptualization, Writing – review & editing. **Yue Qiu:** Investigation, Visualization, Validation. **Qian Zhao:** Investigation, Visualization, Validation. **Zhonghe Wang:** Visualization. **Xiyue Kang:** Visualization. **Linping Yu:** Methodology. **Liang Wu:** Methodology. **Yao Jiang:** Conceptualization, Funding acquisition, Project administration, Supervision, Writing – review & editing, Validation.

Declaration of Competing Interest

The authors declare that they have no known competing financial interests or personal relationships that could have appeared to influence the work reported in this paper.

Data Availability

Data will be made available on request.

Acknowledgements

This work was supported by the National Natural Science Foundation of China (51971251), Postgraduate Scientific Research Innovation Project of Hunan Province (CX20220096).

Appendix A. Supporting information

Supplementary data associated with this article can be found in the

online version at [doi:10.1016/j.apcatb.2023.123386](https://doi.org/10.1016/j.apcatb.2023.123386).

References

- [1] J.A. Turner, Sustainable hydrogen production, *Science* 305 (2004) 972–974, <https://doi.org/10.1126/science.1103197>.
- [2] S. Mallapaty, How China could be carbon neutral by mid-century, *Nature* 586 (2020) 482–483, <https://doi.org/10.1038/d41586-020-02927-9>.
- [3] Z.W. Seh, J. Kibsgaard, C.F. Dickens, I. Chorkendorff, J.K. Nørskov, T.F. Jaramillo, Combining theory and experiment in electrocatalysis: insights into materials design, *Science* 355 (2017) eaad4998, <https://doi.org/10.1126/science.aad4998>.
- [4] X. Wu, Z. Wang, D. Zhang, Y. Qin, M. Wang, Y. Han, T. Zhan, B. Yang, S. Li, J. Lai, L. Wang, Solvent-free microwave synthesis of ultra-small Ru-Mo₂C@CNT with strong metal-support interaction for industrial hydrogen evolution, *Nat. Commun.* 12 (2021) 4018, <https://doi.org/10.1038/s41467-021-24322-2>.
- [5] Y. Wang, G. Qian, Q. Xu, H. Zhang, F. Shen, L. Luo, S. Yin, Industrially promising IrNi-FeNi₃ hybrid nanosheets for overall water splitting catalysis at large current density, *Appl. Catal. B*, 286 (2021), 119881, <https://doi.org/10.1016/j.apcatb.2021.119881>.
- [6] T.I. Singh, G. Rajeshkhan, U.N. Pan, T. Kshetri, H. Lin, N.H. Kim, J.H. Lee, Alkaline Water Splitting Enhancement by MOF-Derived Fe-Co-Oxide/Co@NC-mNS Heterostructure: Boosting QER and HER through Defect Engineering and In Situ Oxidation, *Small* 17 (2021), 2101312, <https://doi.org/10.1002/smll.202101312>.
- [7] M. Li, H. Wang, W. Zhu, W. Li, C. Wang, X. Lu, RuNi Nanoparticles Embedded in N-Doped Carbon Nanofibers as a Robust Bifunctional Catalyst for Efficient Overall Water Splitting, *Adv. Sci.* 7 (2020), 1901833, <https://doi.org/10.1002/advs.201901833>.
- [8] N.K. Oh, J. Seo, S. Lee, H.-J. Kim, U. Kim, J. Lee, Y.-K. Han, H. Park, Highly efficient and robust noble-metal free bifunctional water electrolysis catalyst achieved via complementary charge transfer, *Nat. Commun.* 12 (2021) 4606, <https://doi.org/10.1038/s41467-021-24829-8>.
- [9] J. Sun, N. Guo, T. Song, Y.-R. Hao, J. Sun, H. Xue, Q. Wang, Revealing the interfacial electron modulation effect of CoFe alloys with CoC_x encapsulated in N-doped CNTs for superior oxygen reduction, *Adv. Powder Mater.* 1 (2022), 100023, <https://doi.org/10.1016/j.apmate.2021.11.009>.
- [10] W. Hao, D. Yao, Q. Xu, R. Wang, C. Zhang, Y. Guo, R. Sun, M. Huang, Z. Chen, Highly efficient overall-water splitting enabled via grafting boron-inserted Fe-Ni solid solution nanosheets onto unconventional skeleton, *Appl. Catal. B* 292 (2021), 120188, <https://doi.org/10.1016/j.apcatb.2021.120188>.
- [11] B. You, Y. Zhang, P. Yin, Y. Sun D.-e. Jiang, Universal molecular-confined synthesis of interconnected porous metal oxides-N-C frameworks for electrocatalytic water splitting, *Nano Energy* 48 (2018) 600–606, <https://doi.org/10.1016/j.nanoen.2018.04.009>.
- [12] J. Joo, T. Kim, J. Lee, S.I. Choi, K. Lee, Morphology-controlled metal sulfides and phosphides for electrochemical water splitting, *Adv. Mater.* 31 (2019), 1806682, <https://doi.org/10.1002/adma.201806682>.
- [13] Y. Yu, J. Zhou, Z. Sun, Novel 2D transition-metal carbides: ultrahigh performance electrocatalysts for overall water splitting and oxygen reduction, *Adv. Funct. Mater.* 30 (2020), 2000570, <https://doi.org/10.1002/adfm.202000570>.
- [14] Y. Lu, Z. Li, Y. Xu, L. Tang, S. Xu, D. Li, J. Zhu, D. Jiang, Bimetallic Co-Mo nitride nanosheet arrays as high-performance bifunctional electrocatalysts for overall water splitting, *Chem. Eng. J.* 411 (2021), 128433, <https://doi.org/10.1016/j.cej.2021.128433>.
- [15] D. Lai, Q. Kang, F. Gao, Q. Lu, High-entropy effect of a metal phosphide on enhanced overall water splitting performance, *J. Mater. Chem. A* 9 (2021) 17913–17922, <https://doi.org/10.1039/d1ta04755h>.
- [16] Z. Zheng, L. Lin, S. Mo, D. Ou, J. Tao, R. Qin, X. Fang, N. Zheng, Economizing production of diverse 2D layered metal hydroxides for efficient overall water splitting, *Small* 14 (2018), 1800759, <https://doi.org/10.1002/smll.201800759>.
- [17] V. Vij, S. Sultan, A.M. Harzandi, A. Meena, J.N. Tiwari, W.-G. Lee, T. Yoon, K. S. Kim, Nickel-based electrocatalysts for energy-related applications: oxygen reduction, oxygen evolution, and hydrogen evolution reactions, *ACS Catal.* 7 (2017) 7196–7225, <https://doi.org/10.1021/acscatal.7b01800>.
- [18] G.B. Darband, M. Aliofkhazraei, A.S. Rouhaghdam, M.A. Kiani, Three-dimensional Ni-Co alloy hierarchical nanostructure as efficient non-noble-metal electrocatalyst for hydrogen evolution reaction, *Appl. Surf. Sci.* 465 (2019) 846–862, <https://doi.org/10.1016/j.apsusc.2018.09.204>.
- [19] B. Zhang, F. Yang, X. Liu, N. Wu, S. Che, Y. Li, Phosphorus doped nickel-molybdenum aerogel for efficient overall water splitting, *Appl. Catal. B* 298 (2021), 120494, <https://doi.org/10.1016/j.apcatb.2021.120494>.
- [20] J. Balamurugan, T.T. Nguyen, D.H. Kim, N.H. Kim, J.H. Lee, 3D nickel molybdenum oxyselenide (Ni_{1-x}Mo_xOSe) nanoarchitectures as advanced multifunctional catalyst for Zn-air batteries and water splitting, *Appl. Catal. B* 286 (2021), 119909, <https://doi.org/10.1016/j.apcatb.2021.119909>.
- [21] J. Balamurugan, T.T. Nguyen, V. Aravindan, N.H. Kim, J.H. Lee, Highly reversible water splitting cell building from hierarchical 3D nickel manganese oxyphosphide nanosheets, *Nano Energy* 69 (2020), 104432, <https://doi.org/10.1016/j.nanoen.2019.104432>.
- [22] Q. Yu, Z. Zhang, S. Qiu, Y. Luo, Z. Liu, F. Yang, H. Liu, S. Ge, X. Zou, B. Ding, W. Ren, H.-M. Cheng, C. Sun, B. Liu, A Ta-TaS₂ monolith catalyst with robust and metallic interface for superior hydrogen evolution, *Nat. Commun.* 12 (2021) 6051, <https://doi.org/10.1038/s41467-021-26315-7>.
- [23] H. Chen, Y. Gao, L. Ye, Yn Yao, Y. Wei, X. Chen, An ultrathin nickel-based film electrodeposited from a Ni-Tris molecular precursor for highly efficient electrocatalytic water oxidation, *Electrochim. Acta* 283 (2018) 104–110, <https://doi.org/10.1016/j.electacta.2018.06.167>.
- [24] Y. Wang, X. Li, M. Zhang, J. Zhang, Z. Chen, X. Zheng, Z. Tian, N. Zhao, X. Han, K. Zaghib, Y. Wang, Y. Deng, W. Hu, Highly active and durable single-atom tungsten-doped Ni_{0.5}Se_{0.5} nanosheet @ Ni_{0.5}Se_{0.5} nanorod heterostructures for water splitting, *Adv. Mater.* 34 (2022), 2107053, <https://doi.org/10.1002/adma.202107053>.
- [25] J. Wang, M. Zhang, G. Yang, W. Song, W. Zhong, X. Wang, M. Wang, T. Sun, Y. Tang, Heterogeneous bimetallic Mo-NiP_x/Ni₃Y as a highly efficient electrocatalyst for robust overall water splitting, *Adv. Funct. Mater.* 31 (2021), 2101532, <https://doi.org/10.1002/adfm.202101532>.
- [26] Y. Chen, Y. Wang, J. Yu, G. Xiong, H. Niu, Y. Li, D. Sun, X. Zhang, H. Liu, W. Zhou, Underfocus laser induced ni nanoparticles embedded metallic mon microrods as patterned electrode for efficient overall water splitting, *Adv. Sci.* 9 (2022), 2105869, <https://doi.org/10.1002/advs.202105869>.
- [27] H. Zhang, B. Xi, Y. Gu, W. Chen, S. Xiong, Interface engineering and heterometal doping Mo-NiS/Ni(OH)₂ for overall water splitting, *Nano Res.* 14 (2021) 3466–3473, <https://doi.org/10.1007/s12274-021-3557-y>.
- [28] J. Balamurugan, P.M. Austeria, J.B. Kim, E.S. Jeong, H.H. Huang, D.H. Kim, N. Koratkar, S.O. Kim, Electrocatalysts for Zinc-Air Batteries Featuring Single Molybdenum Atoms in a Nitrogen-Doped Carbon Framework, *Adv. Mater.* 35 (2023), e2302625, <https://doi.org/10.1002/adma.202302625>.
- [29] J. Balamurugan, T.T. Nguyen, N.H. Kim, D.H. Kim, J.H. Lee, Novel core-shell Cu-Mo-oxynitride@N-doped graphene nanohybrid as multifunctional catalysts for rechargeable zinc-air batteries and water splitting, *Nano Energy* 85 (2021), 105987, <https://doi.org/10.1016/j.nanoen.2021.105987>.
- [30] X. Ji, Y. Lin, J. Zeng, Z. Ren, Z. Lin, Y. Mu, Y. Qiu, J. Yu, Graphene/MoS₂/FeCoNi(OH)₂ and Graphene/MoS₂/FeCoNiP_x multilayer-stacked vertical nanosheets on carbon fibers for highly efficient overall water splitting, *Nat. Commun.* 12 (2021) 1380, <https://doi.org/10.1038/s41467-021-21742-y>.
- [31] X. Yang, Z. Zhou, Y. Zou, J. Kuang, D. Ye, S. Zhang, Q. Gao, S. Yang, X. Cai, Y. Fang, Interface reinforced 2D/2D heterostructure of Cu-Co oxides/FeCo hydroxides as monolithic multifunctional catalysts for rechargeable/flexible zinc-air batteries and self-powered water splitting, *Appl. Catal., B* 325 (2023), 122332, <https://doi.org/10.1016/j.apcatb.2022.122332>.
- [32] C. Walter, P.W. Menezes, M. Driess, Perspective on intermetallics towards efficient electrocatalytic water-splitting, *Chem. Sci.* 12 (2021) 8603–8631, <https://doi.org/10.1039/disc01901e>.
- [33] W. Yu, Z. Chen, Y. Zhao, Y. Gao, W. Xiao, B. Dong, Z. Wu, L. Wang, An in situ generated 3D porous nanostructure on 2D nanosheets to boost the oxygen evolution reaction for water-splitting, *Nanoscale* 14 (2022) 4566–4572, <https://doi.org/10.1039/d1nr08007e>.
- [34] X. Liu, M. Gong, S. Deng, T. Zhao, T. Shen, J. Zhang, D. Wang, Transforming damage into benefit: corrosion engineering enabled electrocatalysts for water splitting, *Adv. Funct. Mater.* 31 (2021), 2009032, <https://doi.org/10.1002/adfm.202009032>.
- [35] H. Yang, L. Gong, H. Wang, C. Dong, J. Wang, K. Qi, H. Liu, X. Guo, B.Y. Xia, Preparation of nickel-iron hydroxides by microorganism corrosion for efficient oxygen evolution, *Nat. Commun.* 11 (2020) 5075, <https://doi.org/10.1038/s41467-020-18891-x>.
- [36] Y. Liu, X. Liang, L. Gu, Y. Zhang, G.-D. Li, X. Zou, J.-S. Chen, Corrosion engineering towards efficient oxygen evolution electrodes with stable catalytic activity for over 6000 h, *Nat. Commun.* 9 (2018) 2609, <https://doi.org/10.1038/s41467-018-05019-5>.
- [37] F. Yu, H. Zhou, Y. Huang, J. Sun, F. Qin, J. Bao, W.A. Goddard, S. Chen, Z. Ren, High-performance bifunctional porous non-noble metal phosphide catalyst for overall water splitting, *Nat. Commun.* 9 (2018) 2551, <https://doi.org/10.1038/s41467-018-04746-z>.
- [38] T. Li, J. Yin, D. Sun, M. Zhang, H. Pang, L. Xu, Y. Zhang, J. Yang, Y. Tang, J. Xue, Manipulation of Mott-Schottky Ni/CeO₂ Heterojunctions into N-Doped Carbon Nanofibers for High-Efficiency Electrochemical Water Splitting, *Small* 18 (2022), 2106592, <https://doi.org/10.1002/smll.202106592>.
- [39] W. An, B. Gao, S. Mei, B. Xiang, J. Fu, L. Wang, Q. Zhang, P.K. Chu, K. Huo, Scalable synthesis of ant-nest-like bulk porous silicon for high-performance lithium-ion battery anodes, *Nat. Commun.* 10 (2019) 1447, <https://doi.org/10.1038/s41467-019-09510-5>.
- [40] J.N. Haussmann, R. Beltrán-Suero, S. Mebs, V. Hlukhyy, T.F. Fässler, H. Dau, M. Driess, P.W. Menezes, Evolving highly active oxidic iron(III) phase from corrosion of intermetallic iron silicide to master efficient electrocatalytic water oxidation and selective oxygenation of 5-hydroxymethylfurfural, *Adv. Mater.* 33 (2021), 2008823, <https://doi.org/10.1002/adma.202008823>.
- [41] S. Fang, X. Zhu, X. Liu, J. Gu, W. Liu, D. Wang, W. Zhang, Y. Lin, J. Lu, S. Wei, Y. Li, T. Yao, Uncovering near-free platinum single-atom dynamics during electrochemical hydrogen evolution reaction, *Nat. Commun.* 11 (2020) 1029, <https://doi.org/10.1038/s41467-020-14848-2>.
- [42] B. Zhang, X. Zheng, O. Vozny, R. Comin, M. Bajdich, M. García-Melchor, L. Han, J. Xu, M. Liu, L. Zheng, F.P.Gd Arquer, C.T. Dinh, F. Fan, M. Yuan, E. Yassitepe, N. Chen, T. Regier, P. Liu, Y. Li, P.D. Luna, A. Jammohamed, H.L. Xin, H. Yang, A. Vojvodic, E.H. Sargent, Homogeneously dispersed multimetal oxygen-evolving catalysts, *Science* 352 (2016) 333–337, <https://doi.org/10.1126/science.aaf1525>.
- [43] S. Zhao, Y. Wang, J. Dong, C.-T. He, H. Yin, P. An, K. Zhao, X. Zhang, C. Gao, L. Zhang, J. Lv, J. Wang, J. Zhang, A.M. Khattak, N.A. Khan, Z. Wei, J. Zhang, S. Liu, H. Zhao, Z. Tang, Ultrathin metal-organic framework nanosheets for electrocatalytic oxygen evolution, *Nat. Energy* 1 (2016) 16184, <https://doi.org/10.1038/nenergy.2016.184>.

[44] L. Tan, J. Yu, H. Wang, H. Gao, X. Liu, L. Wang, X. She, T. Zhan, Controllable synthesis and phase-dependent catalytic performance of dual-phase nickel selenides on Ni foam for overall water splitting, *Appl. Catal., B* 303 (2022), 120915, <https://doi.org/10.1016/j.apcatb.2021.120915>.

[45] Y. Li, Y.-C. Miao, C. Yang, Y.-X. Chang, Y. Su, H. Yan, S. Xu, Ir nanodots decorated Ni₃Fe nanoparticles for boosting electrocatalytic water splitting, *Chem. Eng. J.* 451 (2022), 138548, <https://doi.org/10.1016/j.cej.2022.138548>.

[46] J. Su, Y. Yang, G. Xia, J. Chen, P. Jiang, Q. Chen, Ruthenium-cobalt nanoalloys encapsulated in nitrogen-doped graphene as active electrocatalysts for producing hydrogen in alkaline media, *Nat. Commun.* 8 (2017) 14969, <https://doi.org/10.1038/ncomms14969>.

[47] Y. Zheng, Y. Jiao, Y. Zhu, L.H. Li, Y. Han, Y. Chen, A. Du, M. Jaroniec, S.Z. Qiao, Hydrogen evolution by a metal-free electrocatalyst, *Nat. Commun.* 5 (2014) 3783, <https://doi.org/10.1038/ncomms4783>.

[48] V.H. Hoa, D.T. Tran, D.C. Nguyen, D.H. Kim, N.H. Kim, J.H. Lee, Molybdenum and Phosphorous Dual Doping in Cobalt Monolayer Interfacial Assembled Cobalt Nanowires for Efficient Overall Water Splitting, *Adv. Funct. Mater.* 30 (2020), 2002533, <https://doi.org/10.1002/adfm.202002533>.

[49] M.A. Ahsan, A.R.P. Santiago, Y. Hong, N. Zhang, M. Cano, E. Rodriguez-Castellon, L. Echegoyen, S.T. Sreenivasan, J.C. Noveron, Tuning of trifunctional NiCu bimetallic nanoparticles confined in a porous carbon network with surface composition and local structural distortions for the electrocatalytic oxygen reduction, oxygen and hydrogen evolution reactions, *J. Am. Chem. Soc.* 142 (2020) 14688–14701, <https://doi.org/10.1021/jacs.0c06960>.

[50] D.C. Nguyen, T.L.L. Doan, S. Prabhakaran, D.T. Tran, D.H. Kim, J.H. Lee, N.H. Kim, Hierarchical Co and Nb dual-doped MoS₂ nanosheets shelled micro-TiO₂ hollow spheres as effective multifunctional electrocatalysts for HER, OER, and ORR, *Nano Energy* 82 (2021), 105750, <https://doi.org/10.1016/j.nanoen.2021.105750>.

[51] Y. Niu, Y. Yuan, Q. Zhang, F. Chang, L. Yang, Z. Chen, Z. Bai, Morphology-controlled synthesis of metal-organic frameworks derived lattice plane-altered iron oxide for efficient trifunctional electrocatalysts, *Nano Energy* 82 (2021), 105699, <https://doi.org/10.1016/j.nanoen.2020.105699>.

[52] Q. Wang, H. Zhao, F. Li, W. She, X. Wang, L. Xu, H. Jiao, Mo-doped Ni₂P hollow nanostructures highly efficient and durable bifunctional electrocatalysts for alkaline water splitting, *J. Mater. Chem. A* 7 (2019) 7636–7643, <https://doi.org/10.1039/c9ta01015g>.

[53] A. Majeed, X. Li, P.-X. Hou, H. Tabassum, L. Zhang, C. Liu, H.-M. Cheng, Monolayer carbon-encapsulated Mo-doped Ni nanoparticles anchored on single-wall carbon nanotube film for total water splitting, *Appl. Catal., B* 269 (2020), 118823, <https://doi.org/10.1016/j.apcatb.2020.118823>.

[54] Z. Qiu, Y. Ma, T. Edvinsson, In operando Raman investigation of Fe doping influence on catalytic NiO intermediates for enhanced overall water splitting, *Nano Energy* 66 (2019), 104118, <https://doi.org/10.1016/j.nanoen.2019.104118>.

[55] Y. Luo, Z. Zhang, F. Yang, J. Li, Z. Liu, W. Ren, S. Zhang, B. Liu, Stabilized hydroxide-mediated nickel-based electrocatalysts for high-current-density hydrogen evolution in alkaline media, *Energy Environ. Sci.* 14 (2021) 4610–4619, <https://doi.org/10.1039/d1ee01487k>.

[56] B. Zhong, P. Kuang, L. Wang, J. Yu, Hierarchical porous nickel supported NiFeO_xH_y nanosheets for efficient and robust oxygen evolution electrocatalyst under industrial condition, *Appl. Catal., B* 299 (2021), 120668, <https://doi.org/10.1016/j.apcatb.2021.120668>.

[57] Q. Ju, R. Ma, Y. Pei, B. Guo, Q. Liu, T. Zhang, M. Yang, J. Wang, Nitrogen-doped carbon spheres decorated with Co_x nanoparticles as multifunctional electrocatalysts for rechargeable Zn-air battery and overall water splitting, *Mater. Res. Bull.* 125 (2020), 110770, <https://doi.org/10.1016/j.materresbull.2020.110770>.

[58] A. Saad, Y. Gao, K.A. Owusu, W. Liu, Y. Wu, A. Ramiere, H. Guo, P. Tsakaras, X. Cai, Ternary Mo₂NiB₂ as a Superior Bifunctional Electrocatalyst for Overall Water Splitting, *Small* 18 (2022), 2104303, <https://doi.org/10.1002/smll.202104303>.

[59] L. Yu, H. Zhou, J. Sun, F. Qin, F. Yu, J. Bao, Y. Yu, S. Chen, Z. Ren, Cu nanowires shelled with NiFe layered double hydroxide nanosheets as bifunctional electrocatalysts for overall water splitting, *Energy Environ. Sci.* 10 (2017) 1820–1827, <https://doi.org/10.1039/C7EE01571B>.

[60] W. Du, Y. Shi, W. Zhou, Y. Yu, B. Zhang, Unveiling the in situ dissolution and polymerization of Mo in Ni₄Mo alloy for promoting the hydrogen evolution reaction, *Angew. Chem. Int. Ed.* 60 (2021) 7051–7055, <https://doi.org/10.1002/anie.202015723>.

[61] J. Dai, Y. Zhu, H.A. Tahini, Q. Lin, Y. Chen, D. Guan, C. Zhou, Z. Hu, H.-J. Lin, T.-S. Chan, C.-T. Chen, S.C. Smith, H. Wang, W. Zhou, Z. Shao, Single-phase perovskite oxide with super-exchange induced atomic-scale synergistic active centers enables ultrafast hydrogen evolution, *Nat. Commun.* 11 (2020) 5657, <https://doi.org/10.1038/s41467-020-19433-1>.

[62] S. Zhang, G. Chen, T. Qu, J. Wei, Y. Yan, Q. Liu, M. Zhou, G. Zhang, Z. Zhou, H. Gao, D. Yao, Y. Zhang, Q. Shi, H. Zhang, A novel aluminum-carbon nanotubes nanocomposite with doubled strength and preserved electrical conductivity, *Nano Res.* 14 (2021) 2776–2782, <https://doi.org/10.1007/s12274-021-3284-4>.

[63] T. Wu, X. Pang, S. Zhao, S. Xu, Z. Liu, Y. Li, F. Huang, One-step construction of ordered sulfur-terminated tantalum carbide mxene for efficient overall water splitting, *Small Struct.* 3 (2022), 2100206, <https://doi.org/10.1002/ssr.202100206>.

[64] H. Ji, L. Zhang, M.T. Pettes, H. Li, S. Chen, L. Shi, R. Piner, R.S. Ruoff, Ultrathin graphite foam: a three-dimensional conductive network for battery electrodes, *Nano Lett.* 12 (2012) 2446–2451, <https://doi.org/10.1021/nl300528p>.

[65] Y. Pan, L. Gong, X. Cheng, Y. Zhou, Y. Fu, J. Feng, H. Ahmed, H. Zhang, Layer-spacing-enlarged MoS₂ superstructural nanotubes with further enhanced catalysis and immobilization for Li-S batteries, *Acs Nano* 14 (2020) 5917–5925, <https://doi.org/10.1021/acsnano.0c01124>.

[66] Y.-Q. Lyu, F. Ciucci, Activating the bifunctionality of a perovskite oxide toward oxygen reduction and oxygen evolution reactions, *ACS Appl. Mater. Interfaces* 9 (2017) 35829–35836, <https://doi.org/10.1021/acsmi.7b10216>.

[67] M. Zhang, G. Jeerh, P. Zou, R. Lan, M. Wang, H. Wang, S. Tao, Recent development of perovskite oxide-based electrocatalysts and their applications in low to intermediate temperature electrochemical devices, *Mater. Today* 49 (2021) 351–377, <https://doi.org/10.1016/j.mattod.2021.05.004>.

[68] T. Wu, E. Song, S. Zhang, M. Luo, C. Zhao, W. Zhao, J. Liu, F. Huang, Engineering metallic heterostructure based on Ni₃N and 2M-MoS₂ for alkaline water electrolysis with industry-compatible current density and stability, *Adv. Mater.* 34 (2022), 2108505, <https://doi.org/10.1002/adma.202108505>.

[69] Z. Huang, Z. Liu, M. Liao, L. Wang, Z. Luo, T.T. Isimjan, X. Yang, Synergistically improved hydrogen evolution by interface engineering of monodispersed Co_{5.47}N/CoMoO₄ hybrid particles on carbon cloth with rich oxygen vacancies, *Chem. Eng. J.* 462 (2023), 142281, <https://doi.org/10.1016/j.cej.2023.142281>.

[70] H. Wang, Z.-n Chen, D. Wu, M. Cao, F. Sun, H. Zhang, H. You, W. Zhuang, R. Cao, Significantly enhanced overall water splitting performance by partial oxidation of Ir through Au modification in core-shell alloy structure, *J. Am. Chem. Soc.* 143 (2021) 4639–4645, <https://doi.org/10.1021/jacs.0c12740>.

[71] H. Guo, Z. Fang, H. Li, D. Fernandez, G. Henkelman, S.M. Humphrey, G. Yu, Rational design of rhodium-iridium alloy nanoparticles as highly active catalysts for acidic oxygen evolution, *Acs Nano* 13 (2019) 13225–13234, <https://doi.org/10.1021/acsnano.9b06244>.

[72] Y.-R. Zheng, J. Vernieres, Z. Wang, K. Zhang, D. Hochfilzer, K. Krempel, T.-W. Liao, F. Presel, T. Altantzis, J. Fatemans, S.B. Scott, N.M. Secher, C. Moon, P. Liu, S. Bals, S.V. Aert, A. Cao, M. Anand, J.K. Nørskov, J. Kibsgaard, I. Chorkendorff, Monitoring oxygen production on mass-selected iridium-tantalum oxide electrocatalysts, *Nat. Energy* 7 (2022) 55–64, <https://doi.org/10.1038/s41560-021-00948-w>.